Biophysical Journal
Article

Biophysical Society

Coexistence and Pattern Formation in Bacterial Mixtures with Contact-Dependent Killing

Liyang Xiong,[1,2] Robert Cooper,[2] and Lev S. Tsimring[2,3,*]
[1]Department of Physics, [2]BioCircuits Institute, and [3]The San Diego Center for Systems Biology, University of California, San Diego, La Jolla, California

ABSTRACT Multistrain microbial communities often exhibit complex spatial organization that emerges because of the interplay of various cooperative and competitive interaction mechanisms. One strong competitive mechanism is contact-dependent neighbor killing enabled by the type VI secretion system. It has been previously shown that contact-dependent killing can result in bistability of bacterial mixtures so that only one strain survives and displaces the other. However, it remains unclear whether stable coexistence is possible in such mixtures. Using a population dynamics model for two interacting bacterial strains, we found that coexistence can be made possible by the interplay of contact-dependent killing and long-range growth inhibition, leading to the formation of various cellular patterns. These patterns emerge in a much broader parameter range than that required for the linear Turing-like instability, suggesting this may be a robust mechanism for pattern formation.

INTRODUCTION

In natural habitats, microorganisms often form multispecies communities with intricate social organization and complex spatial structures (1). The repertoire of interactions among microorganisms is very diverse and includes cooperation (2,3), competition for common resources (4,5), and predation (6–8). One major question drawing significant interest is how different microbial species may stably coexist within a common environment in the presence of competition and predation (4,9). In this work, we address this question theoretically, focusing on one ubiquitous mechanism of bacterial predation: contact-dependent killing of neighboring cells by direct injection of lethal toxins via the type VI secretion system (T6SS) (10–16). The T6SS has been found in many genera of bacteria, including *Vibrio*, *Pseudomonas*, and *Acinetobacter*.

In a recent work, Borenstein et al. (17) demonstrated that although small micro-colonies of T6SS-sensitive cells are quickly eliminated by surrounding T6SS-active cells, sufficiently large micro-colonies can survive the assault and expand. They explained this size-dependent bifurcation with a purely geometric mechanism. Since the killing occurs on the perimeter of the colony and the growth is in the bulk, the overall balance between killing and growth depends on the colony size. However, these theoretical results predicted no stable coexistence; rather, T6SS inhibition was expected to lead to bistability. Depending on initial conditions, either the T6SS-sensitive or T6SS-active bacteria outcompete the other strain and asymptotically approach a spatially uniform state. The experiments with mixtures of *Escherichia coli* (T6SS-sensitive strain) and *Vibrio cholerae* (T6SS-active strain) indeed showed either growth or shrinkage of localized domains of *E. coli* depending on their initial size. However, the finite time span of the experiments did not allow the authors to see complete elimination of one strain, and thus the question of possible coexistence remained open. McNally et al. (18) also recently studied phase separation in a system of two mutually antagonistic T6SS-active strains of *V. cholerae* and found persistent domain coarsening, which indicates that the stronger strain would eventually win the competition.

In another recent work, Blanchard et al. (19) computationally studied the dynamics of a bacterial population with contact-dependent inhibition such as that mediated by the T6SS. In the well-mixed case, they also found bistability leading to extinction of one strain or the other. On the other hand, they reported that in spatiotemporal simulations, if the diffusion of bacteria was sufficiently slow, two strains could coexist separated by stationary interfaces in a finite parameter domain. However, this effect in their two-component model with bistability could have been a consequence of front pinning that may sometimes occur in coarse finite-difference numerical simulations (20) (see more on this in the Discussion).

Submitted September 12, 2017, and accepted for publication February 2, 2018.

*Correspondence: ltsimring@ucsd.edu

Editor: Zemer Gitai.
https://doi.org/10.1016/j.bpj.2018.02.012

Although local antagonistic interactions generally lead to phase separation and coarsening via front propagation and thus cannot sustain stable strain coexistence, additional long-range interactions may potentially change this outcome and lead to stable coexistence. In this article, we revisit the possibility of stable coexistence in a binary mixture of T6SS-active and T6SS-sensitive bacteria, taking into consideration the potential effects of long-range growth inhibition. We demonstrate theoretically and numerically, using both continuous deterministic and discrete stochastic models, that the interplay of short-range killing and long-range growth inhibition can indeed stabilize the system in a bimodal state with well-separated patches of different bacterial strains. Furthermore, when diffusion of the inhibitor is fast but finite, stable patterns with a characteristic spatial scale can emerge. Such long-range growth inhibition can plausibly arise in natural settings, since a number of factors that limit colony growth, including resource availability, waste accumulation, and quorum sensing, are mediated by fast-diffusing small molecules (21–23). Long-range growth inhibition can also be forward-engineered using the tools of modern synthetic biology (24), for example, by placing an antibiotic resistance gene under the control of a promoter that is repressed by a fast-diffusing quorum-sensing signal (e.g., *N*-acyl homoserine lactones (AHL)).

METHODS

Continuum deterministic model

We developed a continuum population dynamics model for a binary mixture of two strains of bacteria that grow on a two-dimensional (2D) surface and interact via both short-range contact-dependent killing and long-range growth inhibition. The model is based on the partial differential equations for the area densities of T6SS-sensitive bacteria $n_1(\mathbf{r},t)$ and T6SS-active bacteria $n_2(\mathbf{r},t)$, and on the reaction-diffusion equation for the density of the growth inhibitor $A(\mathbf{r},t)$ in a 2D space, $\mathbf{r}\in\mathbf{R}^2$:

$$\frac{\partial n_1}{\partial t} = \frac{\gamma_1}{1+A} n_1(1-n_1-n_2) - \delta n_1 - \kappa n_1 n_2 + \nabla^2 n_1, \quad (1)$$

$$\frac{\partial n_2}{\partial t} = n_2(1-n_1-n_2) - \delta n_2 + \nabla^2 n_2, \quad (2)$$

and

$$\frac{\partial A}{\partial t} = \gamma_A n_1 - \delta_A A + D_A \nabla^2 A. \quad (3)$$

The first equation describes the logistic growth of the T6SS-sensitive cells, their spontaneous death, killing by colocated T6SS-active cells, and diffusion. Note that the growth rate of T6SS-sensitive strain 1 is reduced by the local concentration of inhibitor $A(\mathbf{r},t)$. We use a simple Hill-like function for the inhibition since the specific form is not qualitatively important. The second equation describes the logistic growth of T6SS-active cells, their spontaneous death, and diffusion. The death rates of both strains are small, and if they move on solid agar, their diffusion rates are also small. Although these parameters can be different for the two strains, that difference is not essential, and we assume them to be equal for simplicity. The third equation describes synthesis, decay, and diffusion of the inhibitor A that reduces the growth rate of species n_1. This model has a typical structure of a reaction-diffusion system. Strictly speaking, bacterial communities are not reaction-diffusion systems since they do not "react" with each other as chemical species, and their motility is often quite different from simple linear diffusion. However, such simplified description of their collective dynamics (growth, death, interactions, and motility) is convenient and may serve as a reasonable first approximation to more realistic models of multistrain bacterial communities.

Here, we assume that A is only produced by n_1 and only inhibits growth of n_1. This interaction of A only with n_1 can be realized in synthetic biology as discussed later. However, in natural environments, it might also be produced by n_2 and inhibit growth of n_2. The analysis of a more general model with A produced by and inhibiting growth of both strains is discussed in the Supporting Material, in which we also allow for different death rates of the two strains. In the analysis and simulations described below, we use Eqs. 1, 2, and 3 for simplicity, but our main conclusions are general. In these equations, all variables and parameters are scaled by the growth rate of species 2, the diffusion constant of both strains, and the maximal total density of bacteria at which the logistic growth saturates. Note that in our model the cell growth saturates in the bulk at sufficiently large density, whereas Borenstein et al. (17) assumed that growth was continuous, with new cells pushing old cells out of the simulation domain once the maximal density was reached. This is an important difference since in the latter case, the faster-growing strain always wins for sufficiently large initial domains, whereas in our system, the outcome is more complex and parameter dependent.

Discrete stochastic model

We also developed a lattice-based, discrete-element model to study the effects of stochasticity on the population dynamics of two bacterial strains. We assume that each site of a square lattice may contain an integer number of T6SS-sensitive and T6SS-active cells (n_1 and n_2, respectively). At every time step, each cell can divide with a probability that is proportional to its growth rate (γ_1 or γ_2, respectively), thereby increasing the occupancy number of the corresponding cell type in that lattice site by one. We assume that each lattice site can only accommodate no more than n_0 cells, so once the total number of cells n_1+n_2 at a certain lattice site reaches n_0, cell division at that site is suspended. To model the short-range cell motility, we allow cells to hop to any of four neighboring lattice sites with rates P_n if that neighboring site has a vacancy. A cell can also spontaneously die with probability proportional to δ, thus reducing the number of cells of its type in its lattice site by one. Finally, type-2 cells can kill type-1 cells with probability proportional to κ if they occupy the same site, thus reducing the occupancy number n_1 by one. All these processes are simulated as independent Markovian events. We also introduce a real-valued inhibitor field A that is defined on the same lattice. It is produced at each lattice site in proportion to the corresponding n_1 value, degrades with rate δ_A, and diffuses with the diffusion constant D_A. The spatiotemporal evolution of A was simulated deterministically using the first-order split-step pseudospectral method. We employed 256 × 256 or 512 × 512 lattices with periodic boundary conditions.

RESULTS

Continuum deterministic theory

Population dynamics without long-range inhibition

Let us first consider the two-species population dynamics without long-range inhibition by assuming $\gamma_A = 0$ and imposing the initial condition $A(\mathbf{r},0) = 0$. Clearly, $A(\mathbf{r},t)$ will then remain zero at all times and can be omitted from consideration. The set of two Eqs. 1 and 2 possesses at

most four fixed points, including the trivial fixed point $n_{1,2} = 0$, two "pure" states in which either $n_1 = 0, n_2 \neq 0$ or $n_1 \neq 0, n_2 = 0$, and a mixed state where both $n_{1,2} \neq 0$. The linear stability analysis (see Supporting Material) shows that if $\delta < 1, \gamma_1$, the trivial state is always unstable, and pure n_1 and n_2 states are stable for sufficiently large and small γ_1, respectively. For intermediate γ_1, at $1 < \gamma_1 < 1 + \kappa(1-\delta)/\delta$, the system is bistable (see Fig. 1 *A*, *blue wedge*). In the following, we will always assume $\gamma_1 > 1$, since the most interesting dynamics occur within this regime. For nonzero γ_A, the bifurcation analysis can be carried out as well (Supporting Material).

In the bistable regime, two subcolonies dominated by species 1 and 2 can coexist by occupying different spatial domains. If these domains contact each other and the diffusion coefficients of the two species are nonzero, smooth fronts will form, separating the domains of different species. These fronts will generally move in either direction depending on the system parameters γ_1, δ, κ. Generally, since $\gamma_1 > 1$ for small killing rate κ, the front propagates in the direction

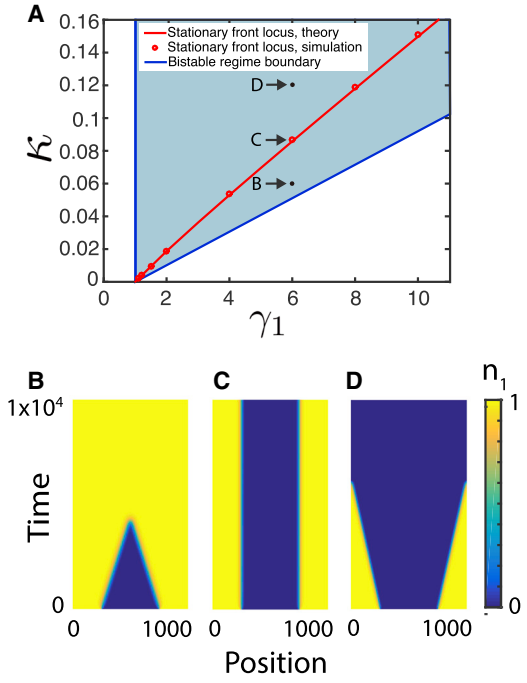

FIGURE 1 (*A*) The blue-shaded wedge in the parameter plane (γ_1, κ) for $\delta = 0.01$ shows the region of bistability in which both pure states are stable and may transiently coexist in space; however, the fronts separating them would generally move in either direction when diffusion is not zero. (*B–D*) demonstrate how one-dimensional fronts reverse direction when κ is increased from 0.06 (*B*) to 0.087 (*C*) to 0.12 (*D*) for $\gamma_1 = 6$ (direct numerical integration of Eqs. 1 and 2). Only the dynamics of n_1 are shown here. In the region where n_1 is high, n_2 is low and vice versa. The red solid line in (*A*), which is plotted according to formula (4), corresponds to the stationary front solution. It separates the parameter regions in which either n_1 or n_2 win the competition. The symbols show the parameter values for which the fronts were indeed found to be stationary in direct simulations. To see this figure in color, go online.

of species 2 and species 1 wins, whereas for sufficiently large κ the front reverses and T6SS-active species 2 wins. For given γ_1 and δ, there is a unique value of κ_s at which the front is stationary. For $\delta, \kappa \ll 1$ it can be found analytically using the so-called Maxwell rule (25) (see Supporting Material for details),

$$\kappa_s = \frac{3\delta(\gamma_1 - 1)^2(\gamma_1^2 - 1 - 2\gamma_1 \ln\gamma_1)}{2\gamma_1^3 + 3\gamma_1^2 - 6\gamma_1 + 1 - 6\gamma_1^2 \ln\gamma_1}. \quad (4)$$

For small $\gamma_1 - 1$, this expression simplifies to $\kappa_s = 2\delta(\gamma_1 - 1)$. Direct numerical simulations of Eqs. 1 and 2 agree well with this formula (Fig. 1).

Infinitely fast inhibitor diffusion

In the limit of infinitely fast inhibitor diffusion $(D_A \to \infty)$, A is spatially uniform, with a magnitude that is dependent on the average concentration of type-1 bacteria over the entire domain: $N_1(t) = \int_C n_1(\mathbf{r}, t)d\mathbf{r}/\mathrm{Area}(C)$. For $\delta_A \gg \delta$, after the initial transient, the magnitude of the inhibitor A becomes slaved to the current value of N_1: $A(t) = \gamma_A N_1(t)/\delta_A$. In the bistable regime, after the phase separation has occurred, $N_1 \approx n_1^* s_1$, where s_1 is the surface area fraction occupied by the type-1 strain and $n_1^* = 1 - \delta(1+A)/\gamma_1$ is at the local fixed point. This yields the self-consistency condition resulting in the relation between s_1 and A:

$$A = \frac{\gamma_1 - \delta}{\frac{\delta_A \gamma_1}{\gamma_A s_1} + \delta}. \quad (5)$$

Now we can use the results of the analysis of the two-variable model with renormalized

$$\gamma_1^* = \gamma_1/(1+A) = (\delta_A \gamma_1 + \delta\gamma_A s_1)/(\delta_A + \gamma_A s_1) \quad (6)$$

instead of γ_1 and determine how the region of bistability will depend on s_1 (see Fig. 2 *A*). The bistability region for arbitrary $0 < s_1 < 1$ is the wedge $1 < \gamma_1^* < 1 + \kappa(1-\delta)/\delta$ (Fig. 2 *A*). Since for each s_1 there is a unique line corresponding to a stationary front, we can also plot a union of all lines $\kappa(\gamma_1)$ by using Eq. 4 with γ_1 replaced by γ_1^* for arbitrary $0 < s_1 < 1$; this union forms a wedge shown in Fig. 2 *B*. Thus, any combination of κ and γ_1 within this wedge can yield a stationary, phase-separated structure with a particular area fraction s_1^*, for which κ and $\gamma_1^*(s_1^*)$ satisfy Eq. 4. Similar results can be obtained in the dual-inhibition model in which both species produce and are inhibited by the same inhibitor (see Supporting Material).

Dynamically, if the parameters κ and γ_1 fall within the domain allowing a stationary front for a certain area fraction s_1^* given by Eqs. 4 and 6, but the initial area fraction of species 1 is smaller than s_1^*, then n_1-domains will expand, and s_1 will increase until it becomes equal to s_1^*, at which time the expansion terminates. Conversely, if $s_1(t=0) > s_1^*$, domains of n_1

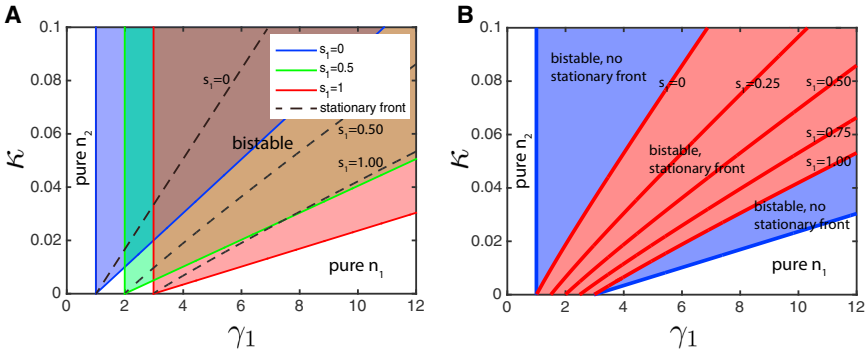

FIGURE 2 (*A*) shows the regions for bistability on (κ, γ_1) plane for three different values of strain 1 area fraction s_1. The blue wedge ($s_1 = 0$) that corresponds to $s_1 = 0$ and $A = 0$ is the same as the one for the two-variable model shown in Fig. 1. (*B*) shows the region of bistability for all values $0 < s_1 < 1$ (*blue wedge*) and the region where fronts would become stationary at specific values of s_1 (*red region*). Parameters are $\delta = 0.01$, $\gamma_A/\delta_A = 2$. To see this figure in color, go online.

will shrink until $s_1 \to s_1^*$. This phase separation with subsequent stabilization of the total area fractions occupied by n_1 and n_2 is easily seen even when $\delta_A/\delta = O(1)$ in numerical simulations of a 2D version of this model starting from random initial conditions (Fig. S5). Fig. S6 shows a comparison of the stationary state of a one-dimensional (1D) system as predicted either analytically using Eqs. 4 and 6 or with direct 1D numerical simulations of the continuum model.

Finite inhibitor diffusion

For large but finite diffusion rate D_A, the approximation of spatially uniform A is only applicable for a sufficiently small system size $L \ll q \equiv \sqrt{D_A/\delta_A}$. In larger systems, the spatial variability of A becomes essential. Furthermore, a finite diffusion rate D_A imposes a characteristic scale for isolated domains of n_1 and n_2. Indeed, consider an isolated island of n_1 in an infinite "sea" of n_2 in 1D (Fig. 3 *A*). This island is a source of inhibitor A that gradually dissipates in the surrounding area. Thus, an island of n_1 generates a localized bump of A, of which the amplitude A_0 depends on the size of the island. If the halfwidth of the island x_0 is much smaller than the inhibitor diffusion scale q, we can neglect the variation of A across the island and obtain the following approximate expression for A_0 valid for small qx_0 (see Supporting Material),

$$A_0 = \frac{\gamma_A}{\delta_A}\left(1 - \delta/\gamma_1^*\right)qx_0. \tag{7}$$

The value of A_0 depends on the size $2x_0$ of the island of n_1. For a very small island, the value of A_0 is also small, γ_1^* is large, and the island will be expanding. For a sufficiently large island, the value of A_0 is also large, the effective growth rate of n_1, γ_1^* will be small, and the island will shrink. The island will neither expand nor shrink if the value of $\gamma_1^* = \gamma_1/(1 + A_0)$ satisfies Eq. 4, which in turn yields a solution for x_0. Comparisons between the width of an isolated spot of n_1 given by this calculation and the direct simulation are illustrated in Fig. 3, *B* and *C* (for these plots, we used a more accurate expression for A_0 than Eq. 7; see Supporting Material). The simulation results are generally consistent with the theory; the slight deviation is because we neglected the variation of A and n_1 across the island. Also, in the simulations, there is a minimal size for stable stationary islands—very small islands shrink and disappear. Reference (17) also pointed out the existence of a critical minimal size of a T6SS-sensitive domain surrounded by T6SS-active cells, but in that work, the mechanism behind it was related to the balance between the bulk growth and perimeter killing, so the bigger the domain, the greater the ratio between the area and the surrounding perimeter. In our model, the bulk growth is saturated at the maximal local density, so the balance between killing and growth is weakly dependent on the area. The existence of the critical minimal domain size is not seen in the analytical results because we neglected the width of the front between n_1 and n_2 in the theory (Fig. 3 *A*). However, in our simulations, for a finite diffusion of n_1 and n_2, the interfaces have a finite width. When

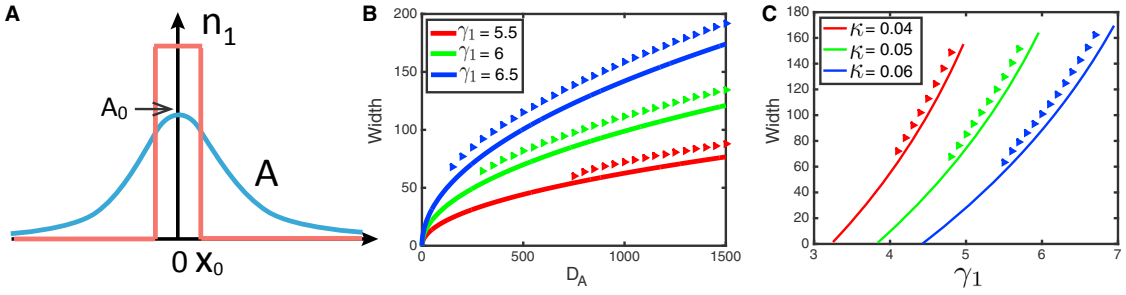

FIGURE 3 (*A*) is a sketch showing the distribution of A produced by a spot of n_1 surrounded by the sea of n_2. (*B* and *C*) show the width of an isolated spot of n_1 as a function of D_A (*B*) and γ_1 (*C*). The curves show the results from theory, and the symbols are from simulations. Parameters are $\delta = 0.01$, $\delta_A = 0.02$, and $\gamma_A = 0.04$. $\kappa = 0.06$ in (*B*), and $D_A = 800$ in (*C*). To see this figure in color, go online.

the size of an island becomes so small that the two finite-width fronts of the island between n_1 and n_2 overlap and annihilate each other, the island collapses.

We also performed simulations of the full three-component deterministic model in 2D, starting from random initial conditions, and observed the formation of quasi-regular patterns of a characteristic size (see Fig. 4). Depending on the parameters, such as the strain-1 growth advantage γ_1 in the case of Fig. 4 *B*, the patterns can manifest as strain-1 islands surrounded by strain 2 or vice versa. For intermediate values of γ_1, labyrinthine patterns are observed.

Turing-like instability

It is well known that an interplay of short-range activation and long-range inhibition is responsible for the onset of the Turing instability (26). We wondered if pattern formation in our system was also the result of a Turing-like instability. Here, indeed, slowly diffusing bacteria n_1 effectively play the role of self-activator by shielding interior cells from the killer strain n_2 and thus promoting their own growth. At the same time, the fast-diffusing field A produced by n_1 acts as an inhibitor for the growth of n_1. When the diffusion constants of activator and inhibitor are sufficiently different, the Turing mechanism manifests itself in the linear instability of a uniform state with respect to small spatially periodic perturbations with finite wavenumbers. To test whether our system indeed exhibits Turing-like instability, we linearized the full model Eqs. 1, 2, and 3 near the mixed state and computed the eigenvalues of spatially periodic perturbations. We indeed found that for certain parameter values, the mixed state is linearly unstable with respect to finite-wavenumber perturbations (Supporting Material).

Fig. 5 *A* shows the region corresponding to the Turing-like instability in the (κ, γ_1) plane for fixed δ, γ_A, δ_A and finite D_A, along with the theoretical lines limiting the region for stationary fronts in the case of infinite D_A, as shown as the red sector in Fig. 2 *B*. As explained above, the existence of such fronts leads to stable pattern formation. The heatmap indicates the values of the wavenumber corresponding to the maximal positive eigenvalue. The Turing-like instability region lies inside the domain allowing stationary fronts, but it is much narrower. Similarly, the region for stable pattern formation obtained numerically from the full nonlinear model Eqs. 1, 2, and 3 for finite inhibitor diffusion is significantly wider than the corresponding Turing-like instability domain (Fig. 5 *B*). These results suggest that pattern formation in this system is a more robust and easily observable phenomenon than linear Turing-like instability of a well-mixed state. Although the Turing-like instability can indeed initiate morphogenesis in this system, the patterns can emerge and stabilize in a much broader range of system parameters because of the nonlinearity of the system. In fact, our numerical simulations show that patterns emerge spontaneously if the two strains are initially well-separated (i.e., there are sufficiently large regions where $n_1 \gg n_2$ or $n_2 \gg n_1$).

Discrete stochastic model

As described in the previous section, the three-component continuum model for the two slowly diffusing bacterial densities and one fast-diffusing growth inhibitor exhibits a pattern-forming Turing-like instability. However, numerical simulations show that stable patterns can exist in a much wider parameter range. We identified a nonlinear mechanism of pattern formation that is based on interface stabilization because of the self-consistent changes in the growth caused by the fast-diffusing inhibitor. This raises the

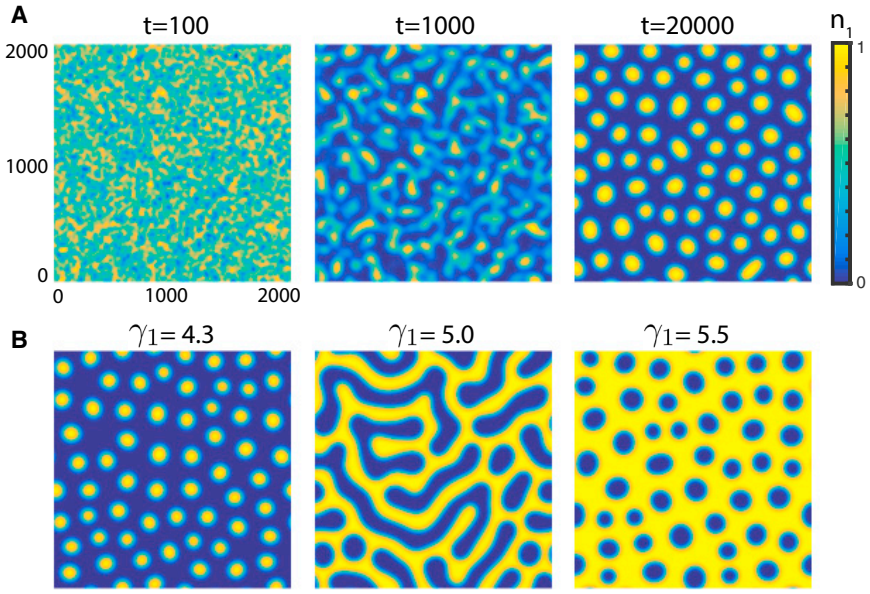

FIGURE 4 Pattern formation in a deterministic model with finite $D_A = 80$ and random initial conditions. (*A*) shows three snapshots of n_1. (*B*) shows snapshots at time $t = 40000$ for different γ_1. $\gamma_1 = 4.5$ in (*A*), and the other parameters are as follows: $\delta = 0.01$, $\kappa = 0.03$, $\gamma_A = 0.04$, and $\delta_A = 0.02$. To see this figure in color, go online.

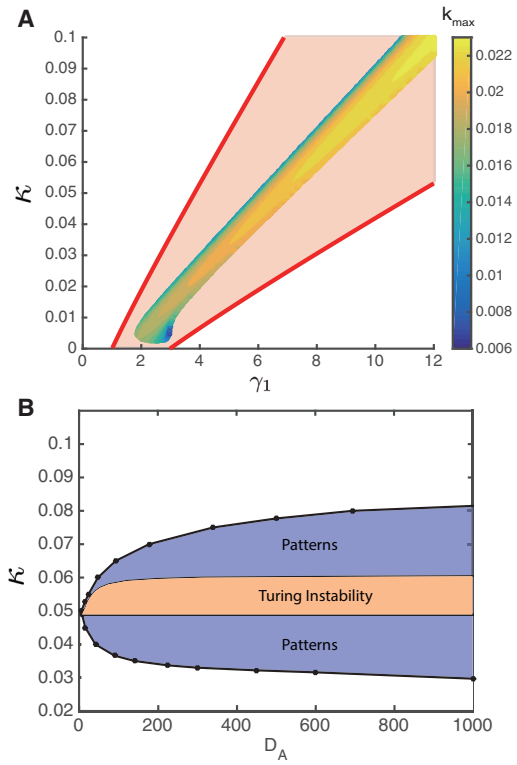

FIGURE 5 The region of the linear Turing-like instability in the $\kappa - \gamma_1$ (A) and $\kappa - D_A$ (B) parameter planes. (A) The heatmap depicts the wavenumber k_{max} corresponding to the maximal positive eigenvalue for the Turing-like instability for $D_A = 500$. The red lines limit the region with stationary fronts and pattern. The parameter values are as follows: (A) $D_A = 500$ and (B) $\gamma_1 = 7$. Other parameters ($\delta = 0.01, \gamma_A = 0.04, \delta_A = 0.02$) are the same for both panels. To see this figure in color, go online.

question of how such well-separated states can emerge from an unpatterned initial condition if it is linearly stable. We note, however, that in an actual experiment, dilute inoculated mixtures would initially grow in conditions that are actually very different from the spatially uniform, well-mixed state that is typically assumed in deterministic reaction-diffusion models. If a mixture was inoculated as a smattering of isolated bacteria that initially have no direct contact, then bacteria of both types would grow for some time, unimpeded by interaction with bacteria of the other type so by the time they begin contacting each other, they would form sufficiently large micro-colonies. This scenario can lead to pattern formation even when the uniformly mixed state is linearly stable.

We used a lattice-based discrete-element model introduced in Methods to simulate this scenario. The simulation results from this model are illustrated by three snapshots of n_1 and n_2 in Fig. S7 A. The initial condition for this simulation was a "dilute mixture" of both strains, so on average only 10% of lattice sites were occupied and typically by no more than a single cell of either type. As seen from the figure, this initial condition eventually gives rise to a patterned state in which spots of n_1 are surrounded by a "sea" of n_2. A characteristic size of the pattern emerges, as evidenced by the narrow-peaked area distribution of n_1 spots (Fig. S7 B). If either inhibitor production is disabled ($\gamma_A = 0$) or neighbor-killing is turned off ($\kappa = 0$), patterns do not form, and either n_1 or n_2 takes over the whole system as the other species is driven to extinction, unless the system parameters are tuned precisely to satisfy the balance condition similar to Eq. 4 (data not shown).

To evaluate the range of parameters in which patterns spontaneously emerge from a dilute initial state, we ran a series of discrete stochastic simulations with a range of values of γ_1 and κ. Again, the initial condition was randomly distributed n_1 and n_2 cells at low concentration. In agreement with the continuum theory, in the bulk of the region where the existence of stable patterns was expected, the patterns indeed spontaneously emerged (see Fig. 6). As seen from this figure, depending on the relative growth advantage of the type-1 strain and the killing efficiency of the type-2 strain, the patterns change their structure: for smaller γ_1/γ_2 or larger κ, they appear as isolated islands of n_1 surrounded by n_2. For large growth advantage of the type-1 strain or small κ, the patterns are reversed: the islands of n_2 are surrounded by the sea of n_1. In the intermediate range, we found more symmetric labyrinthine patterns. We also characterized the observed patterns by the average fraction of n_1 vs. n_2 and the power spectrum of the spatial distribution of n_1 (Fig. S8).

DISCUSSION

Ecological diversity is ubiquitous in nature, ranging in scale from the ecosystems that cover our planet to the microbiome that inhabits our gut. Diversity plays an important role in maintaining the functions of an ecosystem; e.g., the gut microbiome provides many health benefits to its host (27–30). However, the conditions and mechanisms that robustly stabilize this biodiversity are still unclear. To study and explain

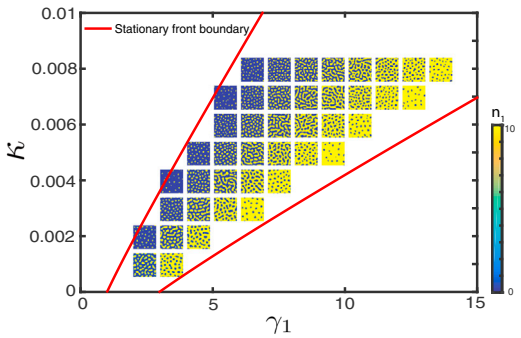

FIGURE 6 Typical patterns emerging from random initial conditions in stochastic simulations for different values of parameters κ and γ_1. Other parameters are as follows: $\gamma_2 = 1$, $n_0 = 10$, $\delta = 0.01$, $\delta_A = 0.02$, $\gamma_A = 0.004$, $P_n = 0.1$, $D_A = 12.5$. The system size is 256×256. Because the number of cells must be integers in stochastic simulations, we use unscaled parameters here. To see this figure in color, go online.

the coexistence of different species within a community, several models have been proposed, such as the rock-paper-scissors game models (31–34). On the other hand, in synthetic biology, stabilization of multistrain microbial communities has proven to be a challenge (35). One recent example of ongoing efforts in this direction is a stable coculture of two different strains with different growth rates in microfluidic chips using a synthetic population control gene circuit (36).

Previous modeling studies of multistrain coexistence used population dynamics equations similar to our work. Frank (37) studied the co-dynamics of bacteriocin-producing strain with bacteriocin-susceptible strain and found that the two species could coexist only when the habitat was spatially heterogeneous. His results can also be readily applied to other mechanisms of contact-dependent killing. In another work, Durrett and Levin (31) studied two-species interactions via colicins and showed that despite the bistability of well-mixed populations, in a spatially structured population only one "stronger" strain will eventually win, depending on system parameters; i.e. neither bistability nor coexistence occurs. This was consistent with previous experimental results (38). On the other hand, Iwasa et al. (39) showed that in relatively small stochastic lattice-type models, a narrow parameter region of bistability may exist, but still without coexistence. Blanchard et al. (19) studied the interaction of two bacterial strains in the presence of contact-dependent killing using a reaction-diffusion-type model and correctly predicted the emergence of bistability that may in principle lead to coexistence of the strains. They also showed through numerical simulations that fronts separating two strains can remain static in a finite parameter range if the diffusion of bacteria is slow enough. However, this latter result has to be taken with the grain of salt because front stabilization in finite-difference simulations may come from pinning. The phenomenon of front pinning in systems with periodic or random inhomogeneities has been studied previously (40–44). Discretization of a continuous reaction-diffusion model in finite-difference numerical integration provides such a periodic structure, which can stop slowly moving fronts (45,46). In our simulations, to minimize pinning artifacts, we used high spatial resolution (512–1024 nodes) and relatively large diffusion constant for bacteria $D_n = 1$. We also verified our simulations by increasing spatial resolution and comparing the results to analytical predictions. The results shown in Fig. 1 demonstrate that our simulations are indeed consistent with continuum theory. However, if we artificially decrease spatial resolution and reduce the diffusion constant in our simulations, we immediately begin to see prominent pinning effects. We performed numerical simulations of the two-variable model without long-range inhibition for small bacterial diffusion $D_n = 0.01$ and different numbers of grid points N_g. Some results of these simulations are shown in Fig. S9. For example, for $N_g = 128$ nodes and a certain value of γ_1, there is a large finite range of κ at which the fronts are stationary, but this range becomes progressively smaller as the number of nodes increases toward the values used in our work.

The coexistence of different species creates the possibility of the emergence of regular patterns. One example is a spiral pattern in the rock-paper-scissors model (34). The balance of local activation and global inhibition has been used to explain many forms of pattern formation, such as self-organized patchiness in ecosystems (47). In another study, nutrient competition and mechanical pushing can drive the occurrence of spatial patterns that can also cycle through hole, labyrinth, and spot patterns (48). The mechanical pushing plays the role of local activation, and nutrient competition assumes the task of global inhibition.

In this article, we demonstrated that a combination of short-range killing with long-range growth inhibition may lead to stable coexistence and pattern formation in mixtures of T6SS-sensitive and T6SS-active bacteria. In the absence of either one of these two mechanisms, one of the two strains eventually takes over, and no stable spatial patterns form. Although the mechanism of pattern formation is similar to the Turing instability, the parameter region for stable coexistence and pattern formation is much broader than the range of the linear Turing-like instability of the uniform mixed state. Thus, in a broad parameter range, the stable patterns may coexist with stable uniform states, and the final outcome depends on the initial conditions. If cells of both types are initially well separated, the system evolves toward stable patterns. In experiments, this would correspond to an initially dilute bacterial inoculum where individual cells are not in direct contact, allowing them to develop into patches (micro-colonies) before making contact with each other. We performed simulations of a lattice-based discrete stochastic model that incorporates cell growth, death, diffusion, neighbor killing, and growth inhibition, and indeed found that patterns emerge spontaneously from an initially dilute state for a broad range of parameters, as predicted by the theory.

In our continuous model, the motion of bacterial cells is described by diffusion terms. In reality, bacterial cells do not simply diffuse like Brownian particles. For example, T6SS-sensitive motile *E. coli* cells perform a run-and-tumble random walk, and T6SS-active bacteria *Acinetobacter baylyi* move on agar surface through twitching using their pili (49). Furthermore, when bacteria form dense communities such as biofilms, cells push each other, and so mechanical stress plays an important role in cell motility and overall colony organization (50–52). In addition, cell motion and growth of real biofilms are affected by cell-cell adhesion and secretion of extracellular matrix (53). None of these factors are included explicitly in our model. Instead, we use diffusion as a simple but reasonable approximation of the cell motility as many researchers have done previously (54–57). In our stochastic lattice model, the cells can jump to neighboring sites only if there is room there.

Still, the results of our stochastic simulations are consistent with the theory and simulations of the deterministic continuum model.

Although we only presented theoretical results here, we anticipate that the mechanism of pattern formation described in this article operates in nature and can be observed in the laboratory. Compared to the Turing instability, this mechanism can produce stable patterns in a much wider parameter range, likely making it easier for experimental verification. In our system, it requires that the T6SS-sensitive bacteria grow faster than T6SS-active ones ($\gamma_1 > 1$) and that the killing rate κ is small. These conditions are not difficult to fulfill. Different bacteria exhibit vastly different growth rates and abilities to metabolize different carbon sources (58–60). For example, in our preliminary experiments, the growth rate of T6SS-sensitive *E. coli* was found to be significantly faster than T6SS-active *A. baylyi*. In the laboratory, we can also vary growth rates by changing carbon sources and/or adding sublethal amounts of antibiotics that selectively slow down growth of different species. The ability of T6SS-active bacteria to kill their neighbors also varies greatly by both the predator and the prey. For example, of three T6SS-active species, *A. baylyi* can kill *V. cholerae*, whereas *A. baylyi* itself succumbs to *Pseudomonas aeruginosa* (61). According to the same study, the T6SS killing rates of these strains are comparable to their division rates if predator and prey cells maintain prolonged contact. However, motile cells are unlikely to have prolonged contacts, so the effective killing rate may be significantly smaller. Furthermore, in laboratory environments, one could tune killing rates in a broad range by knocking out certain T6SS toxic effectors (62), placing key components of the T6SS under an inducible promoter in the predator, or by placing an immunity gene under an inducible promoter in the prey. The death rate used in our model is of the order of 0.01 compared with the growth rate, which is typical in reality (63).

Our model also requires bacteria to produce a long-range inhibitor. As mentioned above, production of fast-diffusing waste or consumption of fast-diffusing nutrients could provide a native mechanism of long-range inhibition. Since bacteria vary in their ability to utilize different carbon sources, it is likely that the degree of growth inhibition within a pair of strains would also differ. However, long-range inhibition could be also forward-engineered using synthetic biology (24). For example, *E. coli* could be endowed with an antibiotic resistance gene controlled by a promoter repressed by a quorum-sensing signal, such as AHL produced by a constitutively expressed AHL-synthase LuxI (64,65). If we add that antibiotic to the media, then as *E. coli* grow and produce more and more AHL, which represses the antibiotic resistance gene, the growth of *E. coli* colonies would gradually slow down. The T6SS-active strain (*A. baylyi*) could be made immune to this antibiotic by constitutively expressing the same resistance gene. Another possible candidate for such long-range inhibitor is colicin, a type of bacteriocin. Some wild-type *E. coli* can produce colicins against closely related bacteria (66–68), but they themselves are usually not affected by their own colicin so long as they express an immunity gene (67). If that immunity gene was knocked out, fast-diffusing colicins would inhibit the growth of *E. coli*. We plan to explore these different possibilities in our future work.

SUPPORTING MATERIAL

Supporting Materials and Methods, nine figures, and four movies are available at http://www.biophysj.org/biophysj/supplemental/S0006-3495(18)30215-7.

AUTHOR CONTRIBUTIONS

L.S.T. designed research. L.X. and L.S.T. performed analytical and numerical calculations. R.C. contributed biological background and expertise. L.X., R.C., and L.S.T. analyzed results and wrote the manuscript.

ACKNOWLEDGMENTS

We thank Igor Aranson, Philip Bittihn, and Jeff Hasty for helpful discussions.

This work was supported by the National Institutes of Health grant R01-GM069811, San Diego Center for Systems Biology (National Insitutes of Health grant P50-GM085764), and the Office of Naval Research (grant N00014-16-1-2093).

REFERENCES

1. Stubbendieck, R. M., C. Vargas-Bautista, and P. D. Straight. 2016. Bacterial communities: interactions to scale. *Front. Microbiol.* 7:1234.
2. Griffin, A. S., S. A. West, and A. Buckling. 2004. Cooperation and competition in pathogenic bacteria. *Nature.* 430:1024–1027.
3. Xavier, J. B., W. Kim, and K. R. Foster. 2011. A molecular mechanism that stabilizes cooperative secretions in Pseudomonas aeruginosa. *Mol. Microbiol.* 79:166–179.
4. Hibbing, M. E., C. Fuqua, …, S. B. Peterson. 2010. Bacterial competition: surviving and thriving in the microbial jungle. *Nat. Rev. Microbiol.* 8:15–25.
5. Rendueles, O., and J.-M. Ghigo. 2015. Mechanisms of competition in biofilm communities. *Microbiol. Spectr.* 3:MB-0009-2014.
6. Stolp, H., and M. P. Starr. 1963. Bdellovibrio bacteriovorus gen. et sp. n., a predatory, ectoparasitic, and bacteriolytic microorganism. *Antonie van Leeuwenhoek.* 29:217–248.
7. Straley, S. C., and S. F. Conti. 1977. Chemotaxis by Bdellovibrio bacteriovorus toward prey. *J. Bacteriol.* 132:628–640.
8. Jürgens, K., and C. Matz. 2002. Predation as a shaping force for the phenotypic and genotypic composition of planktonic bacteria. *Antonie van Leeuwenhoek.* 81:413–434.
9. Coyte, K. Z., J. Schluter, and K. R. Foster. 2015. The ecology of the microbiome: networks, competition, and stability. *Science.* 350:663–666.
10. Pukatzki, S., A. T. Ma, …, J. J. Mekalanos. 2006. Identification of a conserved bacterial protein secretion system in Vibrio cholerae using the Dictyostelium host model system. *Proc. Natl. Acad. Sci. USA.* 103:1528–1533.

11. Leiman, P. G., M. Basler, …, J. J. Mekalanos. 2009. Type VI secretion apparatus and phage tail-associated protein complexes share a common evolutionary origin. *Proc. Natl. Acad. Sci. USA.* 106:4154–4159.
12. Basler, M., M. Pilhofer, …, J. J. Mekalanos. 2012. Type VI secretion requires a dynamic contractile phage tail-like structure. *Nature.* 483:182–186.
13. Pell, L. G., V. Kanelis, …, A. R. Davidson. 2009. The phage λ major tail protein structure reveals a common evolution for long-tailed phages and the type VI bacterial secretion system. *Proc. Natl. Acad. Sci. USA.* 106:4160–4165.
14. de Berardinis, V., D. Vallenet, …, J. Weissenbach. 2008. A complete collection of single-gene deletion mutants of Acinetobacter baylyi ADP1. *Mol. Syst. Biol.* 4:174.
15. Carruthers, M. D., P. A. Nicholson, …, R. S. Munson, Jr. 2013. Acinetobacter baumannii utilizes a type VI secretion system for bacterial competition. *PLoS One.* 8:e59388.
16. Basler, M., and J. J. Mekalanos. 2012. Type 6 secretion dynamics within and between bacterial cells. *Science.* 337:815.
17. Borenstein, D. B., P. Ringel, …, N. S. Wingreen. 2015. Established microbial colonies can survive type VI secretion assault. *PLoS Comput. Biol.* 11:e1004520.
18. McNally, L., E. Bernardy, …, W. C. Ratcliff. 2017. Killing by Type VI secretion drives genetic phase separation and correlates with increased cooperation. *Nat. Commun.* 8:14371.
19. Blanchard, A. E., V. Celik, and T. Lu. 2014. Extinction, coexistence, and localized patterns of a bacterial population with contact-dependent inhibition. *BMC Syst. Biol.* 8:23.
20. Carpio, A., and L. L. Bonilla. 2003. Depinning transitions in discrete reaction-diffusion equations. *SIAM J. Appl. Math.* 63:1056–1082.
21. Matsushita, M., and H. Fujikawa. 1990. Diffusion-limited growth in bacterial colony formation. *Physica A.* 168:498–506.
22. Lazazzera, B. A. 2000. Quorum sensing and starvation: signals for entry into stationary phase. *Curr. Opin. Microbiol.* 3:177–182.
23. Nakano, K., M. Rischke, …, H. Märkl. 1997. Influence of acetic acid on the growth of Escherichia coli K12 during high-cell-density cultivation in a dialysis reactor. *Appl. Microbiol. Biotechnol.* 48:597–601.
24. Khalil, A. S., and J. J. Collins. 2010. Synthetic biology: applications come of age. *Nat. Rev. Genet.* 11:367–379.
25. Maxwell, J. C. 1875. On the dynamical evidence of the molecular constitution of bodies. *Nature.* 11:357–359.
26. Turing, A. M. 1952. The chemical basis of morphogenesis. *Philos. Trans. R. Soc. Lond. B Biol. Sci.* 237:37–72.
27. Bäckhed, F., R. E. Ley, …, J. I. Gordon. 2005. Host-bacterial mutualism in the human intestine. *Science.* 307:1915–1920.
28. Mazmanian, S. K., J. L. Round, and D. L. Kasper. 2008. A microbial symbiosis factor prevents intestinal inflammatory disease. *Nature.* 453:620–625.
29. Lee, Y. K., and S. K. Mazmanian. 2010. Has the microbiota played a critical role in the evolution of the adaptive immune system? *Science.* 330:1768–1773.
30. Dethlefsen, L., and D. A. Relman. 2011. Incomplete recovery and individualized responses of the human distal gut microbiota to repeated antibiotic perturbation. *Proc. Natl. Acad. Sci. USA.* 108 (*Suppl 1*):4554–4561.
31. Durrett, R., and S. Levin. 1997. Allelopathy in spatially distributed populations. *J. Theor. Biol.* 185:165–171.
32. Kerr, B., M. A. Riley, …, B. J. Bohannan. 2002. Local dispersal promotes biodiversity in a real-life game of rock-paper-scissors. *Nature.* 418:171–174.
33. Czárán, T. L., R. F. Hoekstra, and L. Pagie. 2002. Chemical warfare between microbes promotes biodiversity. *Proc. Natl. Acad. Sci. USA.* 99:786–790.
34. Reichenbach, T., M. Mobilia, and E. Frey. 2007. Mobility promotes and jeopardizes biodiversity in rock-paper-scissors games. *Nature.* 448:1046–1049.
35. De Roy, K., M. Marzorati, …, N. Boon. 2014. Synthetic microbial ecosystems: an exciting tool to understand and apply microbial communities. *Environ. Microbiol.* 16:1472–1481.
36. Scott, S. R., M. O. Din, …, J. Hasty. 2017. A stabilized microbial ecosystem of self-limiting bacteria using synthetic quorum-regulated lysis. *Nat. Microbiol.* 2:17083.
37. Frank, S. A. 1994. Spatial polymorphism of bacteriocins and other allelopathic traits. *Evol. Ecol.* 8:369–386.
38. Chao, L., and B. R. Levin. 1981. Structured habitats and the evolution of anticompetitor toxins in bacteria. *Proc. Natl. Acad. Sci. USA.* 78:6324–6328.
39. Iwasa, Y., M. Nakamaru, and S. A. Levin. 1998. Allelopathy of bacteria in a lattice population: competition between colicin-sensitive and colicin-producing strains. *Evol. Ecol.* 12:785–802.
40. Pomeau, Y. 1986. Front motion, metastability and subcritical bifurcations in hydrodynamics. *Physica D.* 23:3–11.
41. Keener, J. P. 1987. Propagation and its failure in coupled systems of discrete excitable cells. *SIAM J. Appl. Math.* 47:556–572.
42. Fáth, G. 1998. Propagation failure of traveling waves in a discrete bistable medium. *Physica D.* 116:176–190.
43. Keizer, J., G. D. Smith, …, J. E. Pearson. 1998. Saltatory propagation of Ca2+ waves by Ca2+ sparks. *Biophys. J.* 75:595–600.
44. Aranson, I. S., B. A. Malomed, …, L. S. Tsimring. 2000. Crystallization kinetics and self-induced pinning in cellular patterns. *Phys. Rev. E Stat. Phys. Plasmas Fluids Relat. Interdiscip. Topics.* 62:R5–R8.
45. Kladko, K., I. Mitkov, and A. R. Bishop. 2000. Universal scaling of wave propagation failure in arrays of coupled nonlinear cells. *Phys. Rev. Lett.* 84:4505–4508.
46. Mitkov, I., K. Kladko, and J. E. Pearson. 1998. Tunable pinning of burst waves in extended systems with discrete sources. *Phys. Rev. Lett.* 81:5453.
47. Rietkerk, M., S. C. Dekker, …, J. van de Koppel. 2004. Self-organized patchiness and catastrophic shifts in ecosystems. *Science.* 305:1926–1929.
48. Xavier, J. B., E. Martinez-Garcia, and K. R. Foster. 2009. Social evolution of spatial patterns in bacterial biofilms: when conflict drives disorder. *Am. Nat.* 174:1–12.
49. Bitrian, M., R. H. González, …, C. B. Nudel. 2013. Blue-light-dependent inhibition of twitching motility in Acinetobacter baylyi ADP1: additive involvement of three BLUF-domain-containing proteins. *Microbiology.* 159:1828–1841.
50. Volfson, D., S. Cookson, …, L. S. Tsimring. 2008. Biomechanical ordering of dense cell populations. *Proc. Natl. Acad. Sci. USA.* 105:15346–15351.
51. Boyer, D., W. Mather, …, L. S. Tsimring. 2011. Buckling instability in ordered bacterial colonies. *Phys. Biol.* 8:026008.
52. Rudge, T. J., P. J. Steiner, …, J. Haseloff. 2012. Computational modeling of synthetic microbial biofilms. *ACS Synth. Biol.* 1:345–352.
53. Nadell, C. D., K. Drescher, and K. R. Foster. 2016. Spatial structure, cooperation and competition in biofilms. *Nat. Rev. Microbiol.* 14:589–600.
54. Golding, I., Y. Kozlovsky, …, E. Ben-Jacob. 1998. Studies of bacterial branching growth using reaction–diffusion models for colonial development. *Physica A.* 260:510–554.
55. Mimura, M., H. Sakaguchi, and M. Matsushita. 2000. Reaction–diffusion modelling of bacterial colony patterns. *Physica A.* 282:283–303.
56. Berg, H. C. 2008. *E. coli* in Motion. Springer-Verlag, New York.
57. Liu, C., X. Fu, …, J. D. Huang. 2011. Sequential establishment of stripe patterns in an expanding cell population. *Science.* 334:238–241.
58. Durot, M., F. Le Fèvre, …, V. Schachter. 2008. Iterative reconstruction of a global metabolic model of Acinetobacter baylyi ADP1 using high-throughput growth phenotype and gene essentiality data. *BMC Syst. Biol.* 2:85.

59. Scott, M., C. W. Gunderson, …, T. Hwa. 2010. Interdependence of cell growth and gene expression: origins and consequences. *Science.* 330:1099–1102.

60. Hermsen, R., H. Okano, …, T. Hwa. 2015. A growth-rate composition formula for the growth of E.coli on co-utilized carbon substrates. *Mol. Syst. Biol.* 11:801.

61. Nelson, M. B., A. B. Chase, …, A. J. Jermy. 2016. The microbial olympics 2016. *Nat. Microbiol.* 1:16122.

62. Ringel, P. D., D. Hu, and M. Basler. 2017. The role of type VI secretion system effectors in target cell lysis and subsequent horizontal gene transfer. *Cell Rep.* 21:3927–3940.

63. Wang, P., L. Robert, …, S. Jun. 2010. Robust growth of Escherichia coli. *Curr. Biol.* 20:1099–1103.

64. Danino, T., O. Mondragón-Palomino, …, J. Hasty. 2010. A synchronized quorum of genetic clocks. *Nature.* 463:326–330.

65. Prindle, A., P. Samayoa, …, J. Hasty. 2011. A sensing array of radically coupled genetic 'biopixels'. *Nature.* 481:39–44.

66. Gillor, O., B. C. Kirkup, and M. A. Riley. 2004. Colicins and microcins: the next generation antimicrobials. *Adv. Appl. Microbiol.* 54:129–146.

67. Riley, M. A., and J. E. Wertz. 2002. Bacteriocins: evolution, ecology, and application. *Annu. Rev. Microbiol.* 56:117–137.

68. Gordon, D., E. Oliver, and J. Littlefield-Wyer. 2007. The diversity of bacteriocins in Gram-negative bacteria. *In* Bacteriocins. Springer, pp. 5–18.

Biophysical Journal, Volume *114*

Supplemental Information

Coexistence and Pattern Formation in Bacterial Mixtures with Contact-Dependent Killing

Liyang Xiong, Robert Cooper, and Lev S. Tsimring

Supporting Material
Coexistence and pattern formation in bacterial mixtures with contact-dependent killing and long-range inhibition

Liyang Xiong,[1,2] Robert Cooper,[2] and Lev S. Tsimring[2,3]

[1] *Department of Physics, University of California, San Diego, La Jolla, California, USA*
[2] *BioCircuits Institute, University of California, San Diego, La Jolla, California, USA*
[3] *The San Diego Center for Systems Biology, UCSD, La Jolla, CA, USA*

I. ANALYSIS OF THE TWO-STRAIN MODEL

We consider the interaction of two strains of bacteria, fast-growing strain 1 with local density $n_1(\mathbf{r},t) and slow-growing strain 2 with local density n_2(\mathbf{r},t)$. The growth of both strains is limited by the total local density of bacteria, so when n_1+n_2 approaches n_0, the growth of both strains saturates. Both strains are characterized by the same death rate δ. Additionally, strain 2 kills strain 1 on direct contact with the rate κ. Both strains are assumed to diffuse horizontally with the same small diffusion constant D_n. The model reads as follows

$$\frac{\partial n_1}{\partial t} = \gamma_1 n_1(1-\frac{n_1+n_2}{n_0}) - \delta n_1 - \kappa n_1 n_2 + D_n\nabla^2 n_1 \tag{S1}$$

$$\frac{\partial n_2}{\partial t} = \gamma_2 n_2(1-\frac{n_1+n_2}{n_0}) - \delta n_2 + D_n\nabla^2 n_2 \tag{S2}$$

In the following, we assume that all parameters $\gamma_1,\gamma_2,\delta,\kappa,D_n,n_0$ are positive. Without loss of generality, we can rescale time $\tilde{t}=\gamma_2 t$, space $\tilde{x}=(\gamma_2/D_n)^{1/2}x$, and densities, $\tilde{n}=n/n_0$, so in rescaled variables $\tilde{\gamma}_2=1,\tilde{\gamma}_1=\gamma_1/\gamma_2,\tilde{\delta}=\delta/\gamma_2,\tilde{\kappa}=\kappa n_0/\gamma_2,\tilde{D}_n=1$. For simplicity, in the following we will drop tildas and keep the same notation for the rescaled variables and parameters:

$$\frac{\partial n_1}{\partial t} = \gamma_1 n_1(1-n_1-n_2) - \delta n_1 - \kappa n_1 n_2 + \nabla^2 n_1 \tag{S3}$$

$$\frac{\partial n_2}{\partial t} = n_2(1-n_1-n_2) - \delta n_2 + \nabla^2 n_2 \tag{S4}$$

Spatially uniform steady states and their stability. This system has four steady states:

1. $n_1 = 1-\frac{\delta}{\gamma_1}, n_2 = 0$.
2. $n_1 = 0$, $n_2 = 1-\delta$.
3. $n_1 = 1-\delta-\frac{\delta}{\kappa}(\gamma_1-1)$, $n_2 = \frac{\delta}{\kappa}(\gamma_1-1)$.
4. $n_1 = n_2 = 0$.

The Jacobian matrix is

$$J = \begin{pmatrix} a_{11} & a_{12} \\ a_{21} & a_{22} \end{pmatrix}$$

with

$$a_{11} = \gamma_1(1-2n_1-n_2) - \delta - \kappa n_2 \tag{S5}$$

$$a_{12} = -\gamma_1 n_1 - \kappa n_1 \tag{S6}$$

$$a_{21} = -n_2 \tag{S7}$$

$$a_{22} = 1-n_1-2n_2-\delta \tag{S8}$$

Steady state 1 has eigenvalues $\lambda_1=\delta-\gamma_1, \lambda_2=(\frac{1}{\gamma_1}-1)\delta$. When $\gamma_1>\delta,1$, it is stable and $n_1>0$. Steady state 2 has eigenvalues $\lambda_1=(\gamma_1-1)\delta-\kappa(1-\delta), \lambda_2=\delta-1$. When $\delta<1$ and $\kappa>\kappa_b=\frac{\delta(\gamma_1-1)}{1-\delta}$, it is stable and $n_2>0$. Steady state 3 is positive when $\gamma_1>1$, $\delta<1$ and $\kappa>\kappa_b$ but is unstable. Trivial steady state 4 is unstable if $\gamma_1>\delta$ or $\delta<1$.

The system is bistable in the range

$$1 < \gamma_1 < 1 + \frac{\kappa(1-\delta)}{\delta} \tag{S9}$$

Stationary front in two-variable model. In the bistable regime, there may exist fronts separating colonies of strains 1 and 2. These fronts generally move in either direction depending on the system parameters. Generally, if $\gamma_1 > 1$, for very small killing rate κ, strain 1 always wins, and the front propagates in the direction of strain 2, while for sufficiently large κ the front reverses. There is a unique value of $\kappa_s = \kappa(\gamma_1, \delta)$ at which the front is stationary. This value of κ_s can be found approximately for small δ and κ, when $n_1 + n_2$ is close to 1 using the Maxwell rule known in thermodynamics.

In the following we assume that $\kappa = \epsilon K$, $\delta = \epsilon\Delta$ with $\epsilon \ll 1$, and introduce new variables

$$N = \epsilon^{-1}(n_1 + n_2 - 1), \quad \xi = n_1 - n_2. \tag{S10}$$

Conversely, $n_1 = (1 + \epsilon N + \xi)/2, n_2 = (1 + \epsilon N - \xi)/2$. In the new variables and in the first order in ϵ, Eqs. (S3),(S4) can be rewritten as

$$\partial_t N = -\frac{N}{2}(\gamma_1 + 1) - \frac{N}{2}(\gamma_1 - 1)\xi - \Delta - \frac{K}{4}(1 - \xi^2) + \nabla^2 N, \tag{S11}$$

$$\epsilon^{-1}\partial_t \xi = -\frac{N}{2}(\gamma_1 - 1) - \frac{N}{2}(\gamma_1 + 1)\xi - \Delta\xi - \frac{K}{4}(1 - \xi^2) + \epsilon^{-1}\nabla^2\xi. \tag{S12}$$

The first equation describes fast relaxation toward the solution

$$N = -\frac{2\left(\Delta + \frac{K}{4}(1 - \xi^2)\right)}{\gamma_1 + 1 + \xi(\gamma_1 - 1)}. \tag{S13}$$

Assuming that the fast initial relaxation has occurred, and N is slaved to slow variably ξ, we can substitute N from Eq. (S13) in Eq. (S12). Returning to the original parameters κ and δ, after simple algebra we get a single reaction-diffusion equation for the slow dynamics of ξ,

$$\partial_t \xi = f(\xi) + \nabla^2 \xi, \tag{S14}$$

where

$$f(\xi) = \delta \frac{1 - \xi^2}{1 + \Gamma\xi}\left[\Gamma + (\Gamma - 1)(1 - \xi)\frac{\kappa}{4\delta}\right] \tag{S15}$$

with $\Gamma = (\gamma_1 - 1)/(\gamma_1 + 1)$. For small δ and κ, this equation describes slow front propagation. Function $f(\xi)$ has two roots $\xi_{1,2} = \pm 1$ corresponding to stable fixed points of Eq. (S14), and an intermediate root at $\Gamma + (\Gamma - 1)(1 - \xi)\frac{\kappa}{4\delta} = 0$ corresponding to an unstable fixed point. Maxwell rule states that a front solution of the 1-D reaction-diffusion equation (S14) connecting stable fixed points ξ_1 and ξ_2 is stationary if $\int_{\xi_1}^{\xi_2} f(\xi) d\xi = 0$.

For $\Gamma \ll 1$, we can drop $\Gamma\xi$ in the denominator of (S15). Then it becomes a cubic polynomial, and it is evident that the integral will be zero if $f(\xi)$ is anti-symmetric with respect to zero, i.e. when intermediate root is $\xi = 0$, or $\Gamma + (\Gamma - 1)\frac{\kappa}{4\delta} = 0$, which gives

$$\frac{\kappa}{\delta} = 2(\gamma_1 - 1). \tag{S16}$$

For finite Γ, integration of the full function (S15) yields the following expression for the ratio κ/δ at which the front is stationary,

$$\frac{\kappa}{\delta} = \frac{3(\gamma_1 - 1)^2(\gamma_1^2 - 1 - 2\gamma_1 \ln \gamma_1)}{2\gamma_1^3 + 3\gamma_1^2 - 6\gamma_1 + 1 - 6\gamma_1^2 \ln \gamma_1}. \tag{S17}$$

It is easy to check that expression (S17) reduces to (S16) for small $\gamma_1 - 1$.

II. ANALYSIS OF THE THREE-VARIABLE MODEL

The full model with long-range inhibition reads as follows

$$\frac{\partial n_1}{\partial t} = \frac{\gamma_1}{1+A/A_0} n_1 \left(1 - \frac{n_1+n_2}{n_0}\right) - \delta n_1 - \kappa n_1 n_2 + D_n \nabla^2 n_1, \tag{S18}$$

$$\frac{\partial n_2}{\partial t} = \gamma_2 n_2 \left(1 - \frac{n_1+n_2}{n_0}\right) - \delta n_2 + D_n \nabla^2 n_2, \tag{S19}$$

$$\frac{\partial A}{\partial t} = \gamma_A n_1 - \delta_A A + D_A \nabla^2 A. \tag{S20}$$

Use the same scaling as above and $\tilde{A} = A/A_0, \tilde{\gamma}_A = \gamma_A n_0/(\gamma_2 A_0), \tilde{\delta}_A = \delta_A/\gamma_2, \tilde{D}_A = D_A/D_n$, we have

$$\frac{\partial n_1}{\partial t} = \frac{\gamma_1}{1+A} n_1(1-n_1-n_2) - \delta n_1 - \kappa n_1 n_2 + \nabla^2 n_1 \tag{S21}$$

$$\frac{\partial n_2}{\partial t} = n_2(1-n_1-n_2) - \delta n_2 + \nabla^2 n_2 \tag{S22}$$

$$\frac{\partial A}{\partial t} = \gamma_A n_1 - \delta_A A + D_A \nabla^2 A \tag{S23}$$

where we again drop tildes for simplicity of notation.

Bifurcation analysis of the spatially uniform steady states. Full three-variable system possesses at most 5 real spatially uniform steady states:

1. $n_1 = \frac{\gamma_1-\delta}{\frac{\delta\gamma_A}{\delta_A}+\gamma_1}, n_2 = 0, A = \frac{\gamma_1-\delta}{\delta+\frac{\gamma_1\delta_A}{\gamma_A}}$.
2. $n_1 = 0, n_2 = 1-\delta, A = 0$.
3. $n_1 = \frac{-b+\sqrt{b^2-4ac}}{2a}, n_2 = 1-n_1-\delta, A = \frac{\gamma_A}{\delta_A} n_1$ where $a = \frac{\kappa\gamma_A}{\delta_A}, b = \kappa - \frac{\gamma_A}{\delta_A}[\delta + \kappa(1-\delta)], c = (\gamma_1-1)\delta - \kappa(1-\delta)$.
4. $n_1 = \frac{-b-\sqrt{b^2-4ac}}{2a}, n_2 = 1-n_1-\delta, A = \frac{\gamma_A}{\delta_A} n_1$ where a, b, c are the same as those in steady state 3.
5. $n_1 = 0, n_2 = 0, A = 0$.

The Jacobian matrix for the system is

$$J = \begin{pmatrix} a_{11} & a_{12} & a_{13} \\ a_{21} & a_{22} & a_{23} \\ a_{31} & a_{32} & a_{33} \end{pmatrix}$$

with

$$\begin{aligned} a_{11} &= \frac{\gamma_1}{1+A}(1-2n_1-n_2) - \delta - \kappa n_2 \\ a_{12} &= -\frac{\gamma_1}{1+A} n_1 - \kappa n_1 \\ a_{13} &= -\frac{\gamma_1}{(1+A)^2} n_1(1-n_1-n_2) \\ a_{21} &= -n_2 \\ a_{22} &= 1-n_1-2n_2-\delta \\ a_{23} &= 0 \\ a_{31} &= \gamma_A \\ a_{32} &= 0 \\ a_{33} &= -\delta_A. \end{aligned}$$

The trivial fixed point 5 is always unstable, and we will not consider it below. The steady states of n_1, n_2 vs. κ with their stability are illustrated in Fig. S1(A),(B). When γ_1 is smaller than a threshold γ_{1c}, steady states 3 and 4 always exist although steady state 3 is non-physical in this case (it corresponds to negative n_2) [Fig. S1(C) left]. At the critical value $\gamma_1 = \gamma_{1c}$, a codimension-2 bifurcation occurs when steady state 2 overlaps with steady states

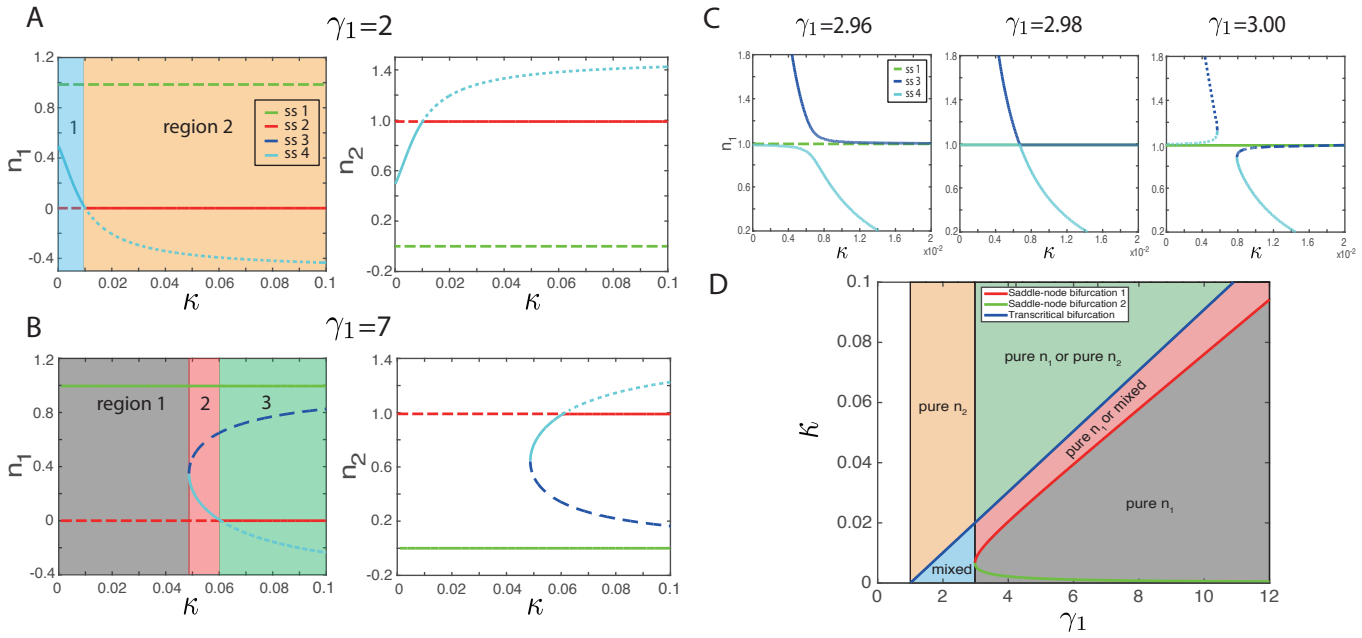

FIG. S1: (A),(B) Steady states of n_1 and n_2 for different γ_1 and κ. Solid lines correspond to stable solutions, long-dashed to unstable solutions, and short-dashed to non-physical steady states for which either n_1 or n_2 are negative. (C) Codimension-2 bifurcation at $\gamma_{1c} = 2.98$. when two saddle-node bifurcation points are born at certain γ_1 and κ and pure solution $n_1 \neq 0, n_2 = 0$ changes stability. (D) Domains of different stable steady states in the (γ_1, κ) parameter plane. Other parameters: $\delta = 0.01, \gamma_A = 0.04, \delta_A = 0.02$.

3 and 4 and two saddle-node bifurcation points emerge [Fig. S1(C) middle]. When $\gamma_1 > \gamma_{1c}$, there are two isolated saddle-node bifurcation points in which steady states 3 and 4 merge and disappear [Fig. S1(C) right].

The condition for the saddle-node bifurcation is $b^2 - 4ac = 0$, which leads to the equation for bifurcation values of $\kappa = \kappa_s$,

$$[1 + \frac{\gamma_A}{\delta_A}(1-\delta)]^2\kappa_s^2 - 2\frac{\gamma_A\delta}{\delta_A}[2\gamma_1 - 1 - \frac{\gamma_A}{\delta_A}(1-\delta)]\kappa_s + \left(\frac{\gamma_A\delta}{\delta_A}\right)^2 = 0, \tag{S24}$$

and thus

$$\kappa_{s\pm} = \frac{\gamma_A\delta}{\delta_A}\left\{\frac{2\gamma_1 - 1 - \frac{\gamma_A}{\delta_A}(1-\delta) \pm 2\sqrt{\gamma_1^2 - \gamma_1[1 + \frac{\gamma_A}{\delta_A}(1-\delta)]}}{[1 + \frac{\gamma_A}{\delta_A}(1-\delta)]^2}\right\}. \tag{S25}$$

From Eq. (S25), it can be shown that $\kappa_{s\pm}$ are real only when

$$\gamma_1 > \gamma_{1c} = 1 + \frac{\gamma_A}{\delta_A}(1-\delta). \tag{S26}$$

We also notice that there is a transcritical bifurcation between steady states 2 and 4 [Fig. S1(A)(B)]. At the transcritical bifurcation point, $n_1 = 0$ which leads to $c = 0$, and thus

$$\kappa = \kappa_t = \frac{\delta(\gamma_1 - 1)}{1 - \delta}. \tag{S27}$$

It is worth mentioning that if $b > 0$ at $\kappa = \kappa_{s_+}$, the saddle-node bifurcation between steady states 3 and 4 happens at $n_1 < 0$, and then the transcritical bifurcation occurs between steady states 2 and 3 instead of 2 and 4 (an example is shown in Fig. S2). In this case, region 2 in Fig. S1(B) disappears, and only regions 1 and 3 remain.

Domains in the parameter plane (γ_1, κ) corresponding to different spatially-uniform stable steady states are shown in Fig. S1(D).

Localized spot of n_1. Here we find an approximate solution for the width of a stationary spot of n_1 surrounded by the sea of n_2, when the diffusion coefficient of A is large but finite. For that we need to compute the distribution

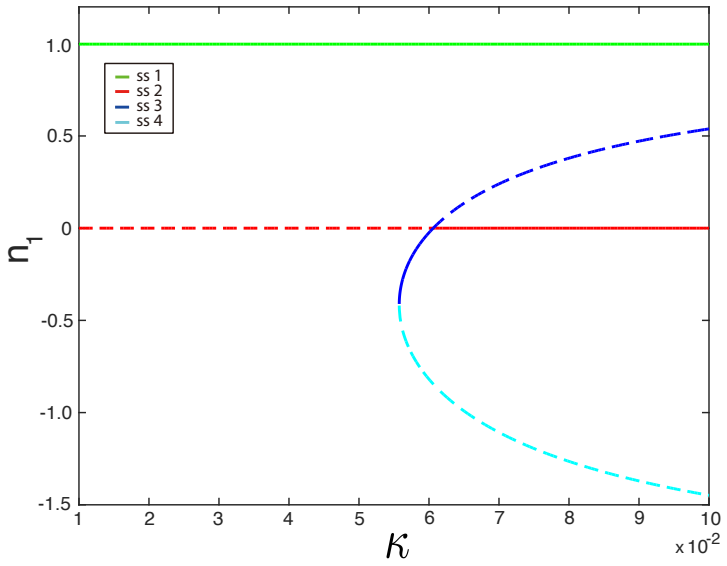

FIG. S2: For sufficiently large γ_1 and small γ_A, the saddle-node bifurcation between steady states 3 and 4 moves to (non-physical) negative n_1, and the transcritical bifurcation occurs between steady states 2 and 3. Parameters: $\gamma_1 = 7, \gamma_A = 0.01$, other parameters are the same as in Fig. S1.

of A produced by such a spot, and find at which spot size the level of A within the spot is such that the interfaces between n_1 and n_2 are stationary. To compute the stationary distribution of A we use Eq. (S23) with $\partial_t A = 0$,

$$\gamma_A n_1 - \delta_A A + D_A \nabla^2 A = 0. \tag{S28}$$

We consider only the 1D case here, but the generalization to 2D is straightforward. We assume that the spot size is much larger than the width of the interfaces separating n_1 and n_2 (which is of the order of $(D_n/\gamma_1)^{1/2}$), but much smaller than the diffusive scale of the inhibitor $q = (\delta_A/D_A)^{1/2}$, and so the spot can be approximated by a rectangular "pulse" with constant $n_1 \approx n_{1*} = 1 - \delta(1 + A(0))/\gamma_1$ for $-x_0 < x < x_0$ and zero outside (see Fig. 3A of the Main text). Solving the Poisson equation (S28) in these two domains and matching A and dA/dx at $x = \pm x_0$, we obtain the following solution for $A(x)$:

$$A(x) = \begin{cases} \frac{\gamma_A}{\delta_A} n_{1*}(1 - e^{-qx_0}\cosh(qx)), & -x_0 < x < x_0 \\ \frac{\gamma_A}{\delta_A} n_{1*} \frac{e^{qx_0} - e^{-qx_0}}{2} e^{-q|x|}, & |x| > x_0 \end{cases} \tag{S29}$$

Substituting $n_{1*} = 1 - \delta(1 + A(0))/\gamma_1$ in Eq. (S29) and take $x = 0$, we can obtain $A(0)$ explicitly,

$$A(0) = \frac{\frac{\gamma_A}{\delta_A}\left(1 - \frac{\delta}{\gamma_1}\right)(1 - e^{-qx_0})}{1 + \frac{\gamma_A \delta}{\gamma_1 \delta_A}(1 - e^{-qx_0})} \tag{S30}$$

The value of A at the front is

$$A(x_0) = \frac{\frac{\gamma_A}{\delta_A}\left(1 - \frac{\delta}{\gamma_1}\right)(1 - e^{-qx_0}\cosh(qx_0))}{1 + \frac{\gamma_A \delta}{\gamma_1 \delta_A}(1 - e^{-qx_0})} \tag{S31}$$

For large inhibitor diffusion, $qx_0 \ll 1$, the difference between $A(0)$ and $A(x_0)$ is small, these expressions can be further simplified to

$$A(0) \approx A(x_0) \approx \frac{\gamma_A}{\delta_A}\left(1 - \frac{\delta}{\gamma_1}\right) qx_0, \tag{S32}$$

which shows that for small x_0 the magnitude of A bump is proportional to x_0, as expected. The spot will be neither expanding nor shrinking if the value of $\gamma_1^* = \gamma_1/(1 + A(x_0))$ with $A(x_0)$ from (S31) satisfies Eq. (S17), which yields the equation for x_0.

Turing-like instability. To explore the possibility of a linear Turing-like instability in our three-component system, we linearized Eqs. (S21)-(S23) near relevant fixed points and studied the eigenvalues corresponding to spatially-periodic perturbations $\sim \exp(ikx + \lambda t)$. Each fixed point has three eigenvalues. Fig. S3 shows three examples of maximal eigenvalues of relevant steady states in different parameter regions [regions 1, 2 and 3 in Fig. S1(B)] vs. wave number k. The middle panel ($\kappa = 0.053$) indeed demonstrates the occurrence of the Turing-like instability when steady state 4 is unstable with respect to small perturbations within a finite range of wavenumbers. The right panel ($\kappa = 0.07$) shows the situation when the fixed point is unstable with respect to spatially uniform as well as spatially-periodic perturbations, but the maximal growth rate occurs at a finite wavenumber. Our numerical simulations show that stable patterns are also possible in this parameter range.

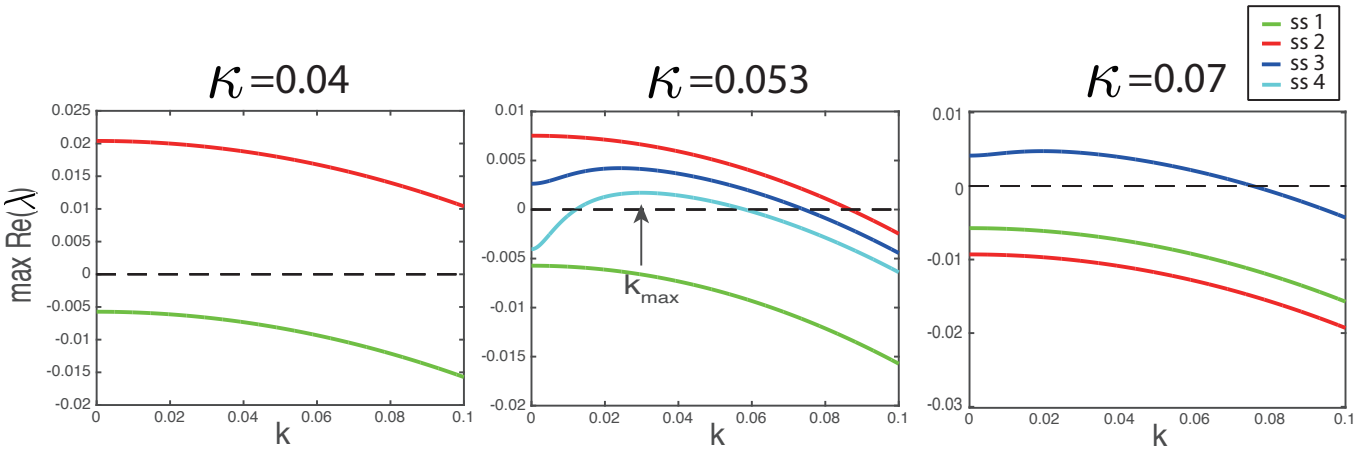

FIG. S3: Maximal real parts of eigenvalues of different steady states in different regions (regions 1, 2 and 3) in Fig. S1(B) vs. wave number k. Parameters are $\gamma_1 = 7, \delta = 0.01, \gamma_A = 0.04, \delta_A = 0.02, D_A = 100$.

III. DUAL-INHIBITION MODEL

To formulate the model considered in the Main text, we assumed that the long-range inhibitor A was only produced by the T6SS-sensitive strain, and only affected its own growth. To generalize this model, here we assume that A is produced by both n_1 and n_2 and it also can inhibit the growth rates of both strains, although not necessarily equally. Furthermore, here we allow strains to have different death rates δ_1 and δ_2. We still assume that both strains have the same diffusion constant for simplicity. Now the model equations read as

$$\frac{\partial n_1}{\partial t} = \frac{\gamma_1}{1+A} n_1(1 - n_1 - n_2) - \delta_1 n_1 - \kappa n_1 n_2 + \nabla^2 n_1, \tag{S33}$$

$$\frac{\partial n_2}{\partial t} = \frac{1}{1+\alpha A} n_2(1 - n_1 - n_2) - \delta_2 n_2 + \nabla^2 n_2, \tag{S34}$$

$$\frac{\partial A}{\partial t} = \gamma_{A1} n_1 + \gamma_{A2} n_2 - \delta_A A + D_A \nabla^2 A. \tag{S35}$$

Similar to the results in the Main text, for infinitely fast inhibitor diffusion, A is spatially-uniform with a magnitude that is now dependent on the mean concentrations of both types of bacteria over the entire domain. If s_1 is the surface area fraction occupied by the type-1 strain, then $n_1^* = 0, n_2^* = 1 - \delta_2(1 + \alpha A)$ and $n_1^* = 1 - \frac{\delta_1}{\gamma_1}(1 + A), n_2^* = 0$ are the two local fixed points. This yields the self-consistency condition resulting in the relation between s_1 and A:

$$s_1 \gamma_{A1}(1 - \frac{\delta_1}{\gamma_1}(1 + A)) + (1 - s_1)\gamma_{A2}(1 - \delta_2(1 + \alpha A)) = \delta_A A, \tag{S36}$$

then

$$A = \frac{s_1\gamma_{A1}(1-\frac{\delta_1}{\gamma_1}) + (1-s_1)\gamma_{A2}(1-\delta_2)}{s_1\gamma_{A1}\frac{\delta_1}{\gamma_1} + (1-s_1)\gamma_{A2}\delta_2\alpha + \delta_A}. \tag{S37}$$

Stationary fronts for infinitely fast inhibitor diffusion. First, we derive the condition for stationary fronts for the generalized two-variable model with $\delta_1 \neq \delta_2$. Since A affects the growth rate of n_2 in the subsequent analysis, we also do not scale out the growth rate of n_2 and write it explicitly as γ_2. Consider the equations

$$\frac{\partial n_1}{\partial t} = \gamma_1 n_1(1-n_1-n_2) - \delta_1 n_1 - \kappa n_1 n_2 + \nabla^2 n_1, \tag{S38}$$

$$\frac{\partial n_2}{\partial t} = \gamma_2 n_2(1-n_1-n_2) - \delta_2 n_2 + \nabla^2 n_2. \tag{S39}$$

We assume that $\kappa = \epsilon K$, $\delta_1 = \epsilon\Delta_1$, $\delta_2 = \epsilon\Delta_2$ with $\epsilon \ll 1$, and again introduce new variables

$$N = \epsilon^{-1}(n_1+n_2-1), \quad \xi = n_1 - n_2. \tag{S40}$$

Conversely, $n_1 = (1+\epsilon N+\xi)/2, n_2 = (1+\epsilon N-\xi)/2$. In new variables and in the first order in ϵ,

$$\partial_t N = -\frac{N}{2}(\gamma_1+\gamma_2) - \frac{N}{2}(\gamma_1-\gamma_2)\xi - \frac{1}{2}(\Delta_1+\Delta_2) - \frac{\xi}{2}(\Delta_1-\Delta_2) - \frac{K}{4}(1-\xi^2) + \nabla^2 N, \tag{S41}$$

$$\epsilon^{-1}\partial_t \xi = -\frac{N}{2}(\gamma_1-\gamma_2) - \frac{N}{2}(\gamma_1+\gamma_2)\xi - \frac{1}{2}(\Delta_1+\Delta_2)\xi - \frac{1}{2}(\Delta_1-\Delta_2) - \frac{K}{4}(1-\xi^2) + \epsilon^{-1}\nabla^2\xi. \tag{S42}$$

The first equation describes fast relaxation toward the solution

$$N = -\frac{(\Delta_1+\Delta_2) + \xi(\Delta_1-\Delta_2) + \frac{K}{2}(1-\xi^2)}{\gamma_1+\gamma_2+\xi(\gamma_1-\gamma_2)}. \tag{S43}$$

Assuming that the fast initial relaxation has occurred, and N is slaved to ξ, we can substitute N from Eq. (S43) in Eq. (S42). Returning to the original parameters κ and $\delta_{1,2}$, after simple algebra we get a single reaction-diffusion equation for the slow dynamics of ξ,

$$\partial_t \xi = f(\xi) + \nabla^2\xi, \tag{S44}$$

where

$$f(\xi) = \frac{1-\xi^2}{1+\Gamma\xi}\left[\frac{\delta_1+\delta_2}{2}\Gamma - \frac{\delta_1-\delta_2}{2} + (\Gamma-1)(1-\xi)\frac{\kappa}{4}\right] \tag{S45}$$

with $\Gamma = (\gamma_1-\gamma_2)/(\gamma_1+\gamma_2)$. For small $\delta_{1,2}$ and κ, this equation describes slow front propagation. Function $f(\xi)$ has two roots $\xi_{1,2} = \pm 1$ corresponding to stable fixed points of Eq. (S44), and an intermediate root at $\frac{\delta_1+\delta_2}{2}\Gamma - \frac{\delta_1-\delta_2}{2} + (\Gamma-1)(1-\xi)\frac{\kappa}{4} = 0$ corresponding to an unstable fixed point. Maxwell rule states that a front solution of the 1-D reaction-diffusion equation (S44) connecting stable fixed points ξ_1 and ξ_2 is stationary if $\int_{\xi_1}^{\xi_2} f(\xi)d\xi = 0$.

For finite Γ, integration of the full function (S45) yields the following expression for κ at which the front is stationary,

$$\kappa = \frac{3(\gamma-1)^2(\gamma^2-1-2\gamma\ln\gamma)}{2\gamma^3+3\gamma^2-6\gamma+1-6\gamma^2\ln\gamma}\left(\frac{\delta_1+\delta_2}{2} - \frac{\delta_1-\delta_2}{2}\frac{\gamma+1}{\gamma-1}\right), \tag{S46}$$

where $\gamma = \gamma_1/\gamma_2$.

Returning to the three-variable model (Eqs. (S33)-(S35)), we notice that for spatially uniform A, the rescaled growth rates are $\gamma_1^* = \frac{\gamma_1}{1+A}$ and $\gamma_2^* = \frac{1}{1+\alpha A}$, and

$$\gamma = \frac{\gamma_1^*}{\gamma_2^*} = \gamma_1\frac{1+\alpha A}{1+A}. \tag{S47}$$

Thus, the fronts become stationary when A is equal to uniform A^* at which γ and κ satisfy Eq. (S46). This value of A^* corresponds to a particular area fraction s_1^* according to Eq. (S37). Thus, the union of the curves defined by Eq. (S46) together with Eqs. (S37) and (S47) when s_1 changes from 0 to 1, will yield the region for stationary fronts where we can expect emergence of patterns.

Stability of stationary fronts. Next we derive the condition for stability of stationary fronts with respect to their uniform displacement. If there is a small front displacement that changes s_1 with respect to s_1^* by a perturbation Δs_1, then the ratio of γ_1/γ_2 changes as well, by $\Delta\gamma = \frac{\partial\gamma}{\partial A}\frac{\partial A}{\partial s_1}\Delta s_1$. It is easy to see that the stationary front is stable if $\Delta s_1 \Delta\gamma < 0$, so for $s_1 > s_1^*$, $\gamma < \gamma^*$, the front moves in the direction that decreases s_1 back to s_1^*. In the opposite case, the front will move in the direction to further increase s_1, and n_1 will win. Thus, the condition for stable stationary fronts is

$$\frac{\partial\gamma}{\partial A}\frac{\partial A}{\partial s_1} = \gamma_1\frac{\alpha-1}{(1+A)^2}\frac{\gamma_{A1}\gamma_{A2}[\alpha\delta_2(1-\frac{\delta_1}{\gamma_1})-\frac{\delta_1}{\gamma_1}(1-\delta_2)]+[\gamma_{A1}(1-\frac{\delta_1}{\gamma_1})-\gamma_{A2}(1-\delta_2))]\delta_A}{[s_1\gamma_{A1}\frac{\delta_1}{\gamma_1}+(1-s_1)\gamma_{A2}\delta_2\alpha+\delta_A]^2} < 0. \tag{S48}$$

If $\delta_1, \delta_2, \gamma_{A1}, \gamma_{A2} \ll 1$, the condition can be simplified to

$$(\alpha-1)(\gamma_{A1}-\gamma_{A2}) < 0. \tag{S49}$$

This means if n_2 produces A faster than n_1 ($\gamma_{A2} > \gamma_{A1}$), for the stationary fronts to be stable, the growth inhibition of n_2 should be stronger ($\alpha > 1$) and vice versa. If $\alpha = 1$, then $\gamma = \gamma_1$ is a constant, and the front is only stationary on a single curve, as in the two-variable model without long-range inhibition.

One example of the region for stationary fronts and pattern formation is shown in Fig. S4.

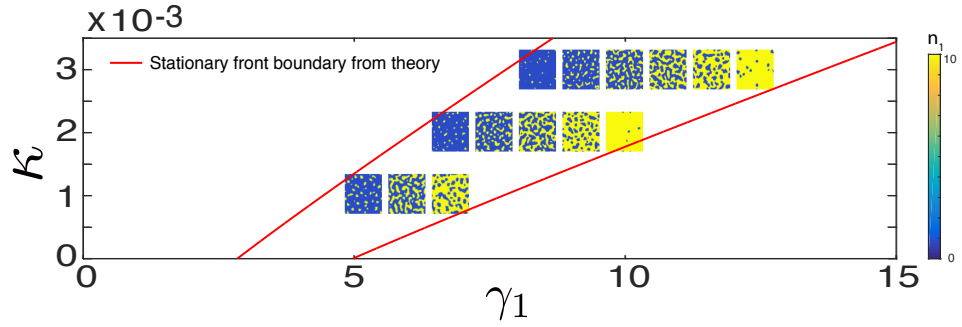

FIG. S4: Typical patterns emerging from random initial conditions in stochastic simulations of the dual-inhibition model for different values of parameters κ and γ_1. Other parameters are $n_0 = 10, \alpha = 0.1, \delta_1 = 0.01, \delta_2 = 0.005, \gamma_{A1} = 0.004, \gamma_{A2} = 0.001, \delta_A = 0.02, D_A = 12.5, P_n = 0.1$. The system size is 256×256.

IV. FRONT PINNING

To address the issue of possible front pinning due to spatial discretization of continuous reaction-diffusion-type models and compare the results with Blanchard et al.[1], we performed 1D simulations of front dynamics in the two-variable model (Eqs. (S3)(S4)), but changed the diffusion constant to a much smaller value $D_n = 0.01$ using different spatial discretizations of the computational domain of fixed length $L = 1024$. The results are shown in Fig. S9. The width of the wedge in the (γ_1, κ) plane in which fronts are stationary decreases exponentially with the number of grid points. When the number of spatial points is 1024, the width of the wedge is so small that it appears as a single line that is consistent with the continuum theory prediction (red curve). However, when the number of spatial points is reduced to 512, the wedge where fronts are stationary appears, which means front pinning. When the number of points is reduced even further, the region for front pinning becomes larger. The fewer number of grid points is equivalent to smaller diffusion constants for the same spatial resolution, thus these results also imply that, as the diffusion constant becomes smaller, the parameter region for pinned fronts increases, which is consistent with Ref. [1]. In our simulations, we used relatively high diffusion constant $D_n = 1$ and a sufficiently large number of grid points to make pinning effects negligible.

V. DETAILS OF THE DISCRETE LATTICE MODEL

In our stochastic simulations, we used a discrete lattice model to simulate strain competition and pattern formation. Specifically, the rules of the model are as follows: the number of cells in each strain is an integer number, so we used

unscaled parameters to carry out the simulations. We use a lattice model to do stochastic simulations, the rules for the simulations are:

1. We consider a square lattice model $0 \leq \{i, j\} \leq N$.

2. The number of individuals of each of the two species n_1, n_2 at each lattice site $\{i, j\}$ is integer, and the sum of $n_1(i, j)$ and$n_2(i, j)$ cannot exceed the maximum carrying capacity n_0.

3. The inhibitor A is defined as a real-valued field on the same lattice.

4. At each time step Δt, $n_1(i, j)$ can increase by one, $[n_1(i, j) \to n_1(i, j) + 1]$, with the probability $\gamma_1 n_1(i, j)[1 - (n_1(i, j) + n_2(i, j))/n_0]\Delta t$ or die $[n_1(i, j) \to n_1(i, j) - 1]$ with the probability $(\delta n_1(i, j) + \kappa n_1(i, j)n_2(i, j))\Delta t$. Similar probabilities apply to n_2 with swapping of subscripts $1 \leftrightarrow 2$ without the killing term.

5. Each cell can jump to one of four neighboring squares with the probability $P_n \Delta t$. The destination site is chosen at random, unless the neighboring site already has n_0 cells, then jumping there is forbidden.

6. We impose periodic boundary conditions in both dimensions for $n_1(i, j), n_2(i, j)$, and $A(i, j)$.

7. Reaction-diffusion dynamics of A is implemented via a split-step pseudo-spectral method.

VI. SUPPLEMENTARY MOVIES

Movie 1 Two-dimensional simulations of the deterministic continuum model with spatially uniform inhibitor A (infinite D_A) and random initial conditions. Parameters: $\gamma_1 = 4.5, \delta = 0.01, \kappa = 0.03, \gamma_A = 0.04, \delta_A = 0.02$.

Movie 2 Two-dimensional simulations of the deterministic continuum model with finite $D_A = 80$ and random initial conditions. Parameters: $\gamma_1 = 4.5, \delta = 0.01, \kappa = 0.03, \gamma_A = 0.04, \delta_A = 0.02$.

Movie 3 Two-dimensional stochastic simulations with random initial conditions. Parameters: $\gamma_1 = 3.5, \gamma_2 = 1, n_0 = 10, \delta = 0.01, \kappa = 0.003, \gamma_A = 0.004, \delta_A = 0.02, P_n = 0.1, D_A = 12.5$.

Movie 4 Two-dimensional stochastic simulations of dual-inhibition model with random initial conditions. Parameters: $\gamma_1 = 6, \gamma_2 = 1, n_0 = 10, \delta_1 = 0.01, \delta_2 = 0.005, \alpha = 0.1, \kappa = 0.001, \gamma_{A1} = 0.004, \gamma_{A2} = 0.001, \delta_A = 0.02, P_{n1} = 0.1, P_{n2} = 0.5, D_A = 12.5$.

[1] Andrew E Blanchard, Venhar Celik, and Ting Lu. Extinction, coexistence, and localized patterns of a bacterial population with contact-dependent inhibition. *BMC Systems Biology*, 8(1):1, 2014.

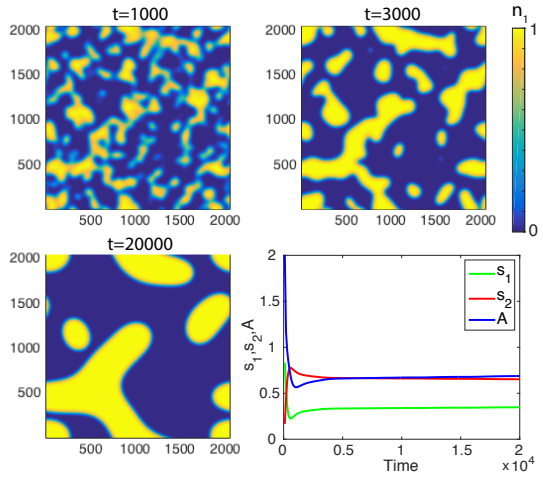

FIG. S5: Phase separation in the deterministic model with spatially uniform inhibitor A (infinite D_A) and random initial conditions. Three snapshots of n_1 and the time course of s_1, s_2 and A for 2D model. At large times, the area fractions s_1 and s_2 approach constant values, and the patterned state stabilizes. Parameters: $\gamma_1 = 4.5$, $\delta = 0.01$, $\kappa = 0.03$, $\gamma_A = 0.04$, $\delta_A = 0.02$.

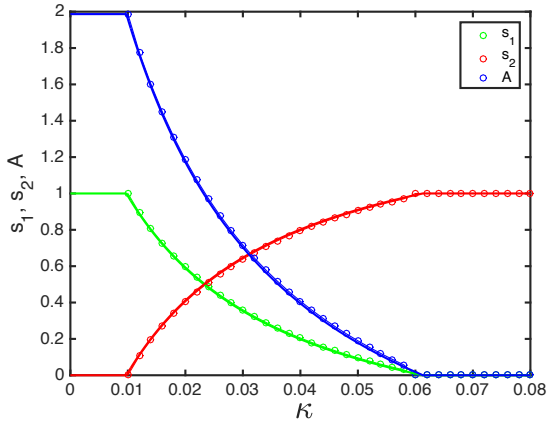

FIG. S6: Final area fractions of the two strains and the inhibitor level A as functions of the killing rate κ in the deterministic 1D model with spatially uniform inhibitor A (infinite D_A) and random initial conditions. The solid curves show the theoretical predictions using Eqs. (4)(6) in the Main text, and the circles show the simulation results. Parameters: $\gamma_1 = 4.5, \delta = 0.01, \gamma_A = 0.04, \delta_A = 0.02$, system size is 4096.

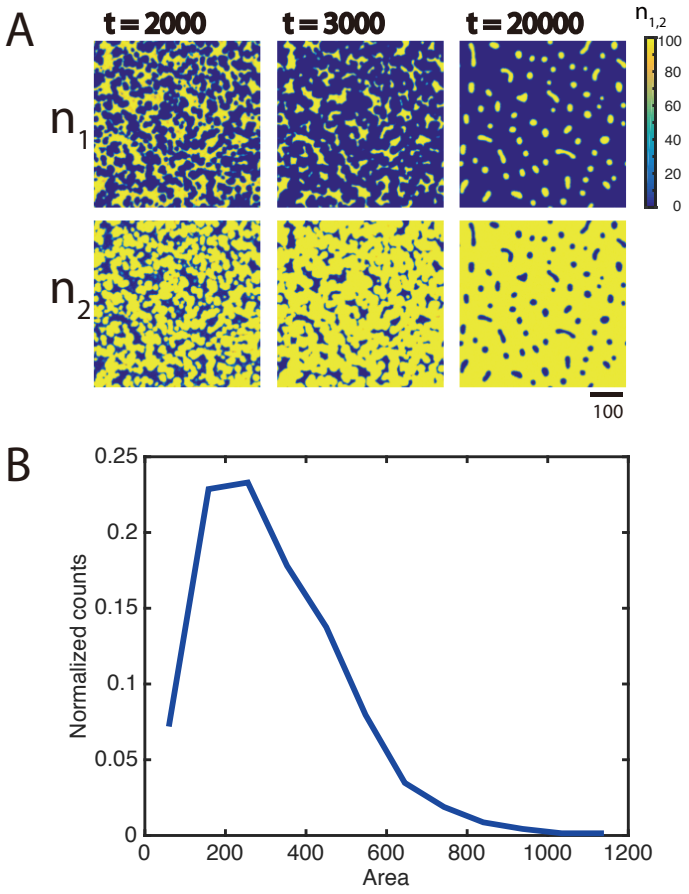

FIG. S7: Discrete stochastic simulations of pattern formation in a mixture of T6SS-sensitive (n_1) and T6SS-active (n_2) bacteria. (A) Three snapshots of a typical simulation. (B) Area distribution of spots of n_1 at $t = 20000$. The distribution result is from 10 stochastic simulations. Parameters: $\gamma_1 = 3, \gamma_2 = 1, n_0 = 100, \delta = 0.01, \gamma_A = 0.0001, \delta_A = 0.005, P_n = 0.04, D_A = 5$ and $\kappa = 0.00025$.

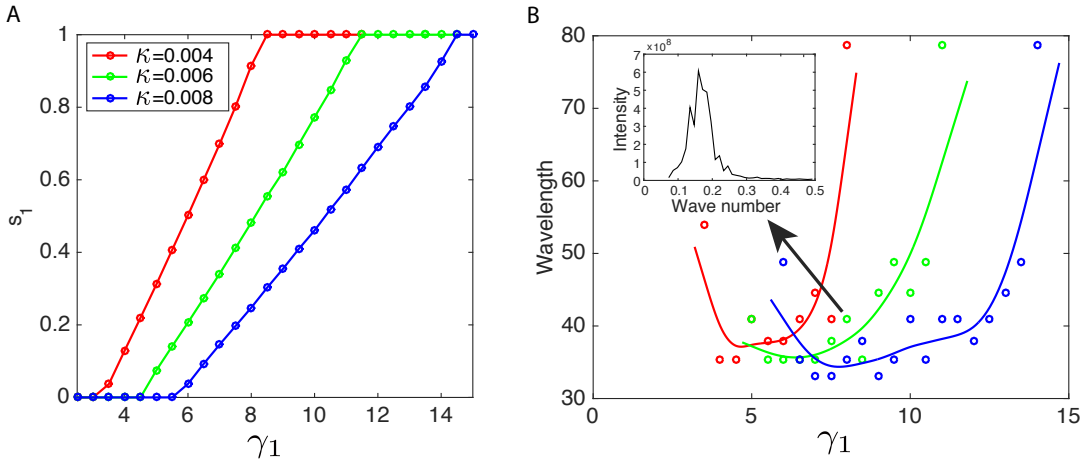

FIG. S8: Analysis of the patterns in stochastic simulations in Fig. 6. (A) n_1 area ratio s_1 vs. γ_1 in stochastic simulations for different κ. The fraction of n_1 changes continuously from 0 to 1 as the control parameter γ_1 moves across the pattern-forming range. (B) Peak wavelength of the asymptotic pattern vs. γ_1 for the same three values of κ as in panel (A). The circles are from simulations. The curves are smoothing spline extrapolated of the circles with the same color. The characteristic scale is diverging near the boundaries of the pattern-forming region in the parameter space. Inset: the power spectrum for $\kappa = 0.006, \gamma_1 = 8$. It has a well-defined peak corresponding to the characteristic distance between the spots or the period of the labyrinthine pattern.

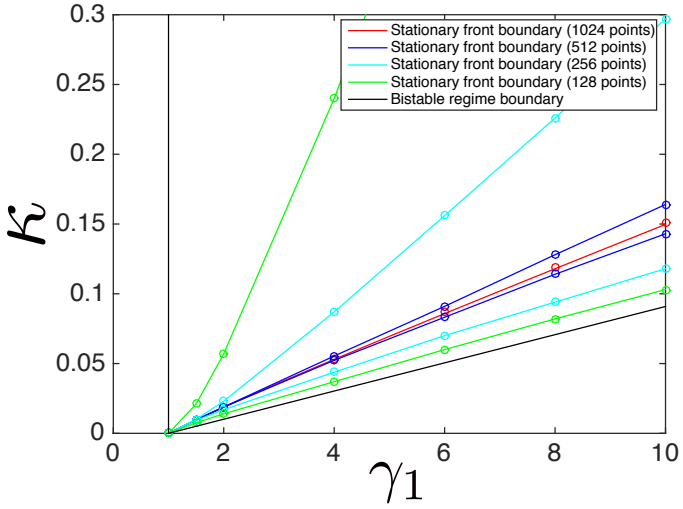

FIG. S9: Coarse spatial discretization leads to front pinning in finite-difference numerical simulations. Different lines show the simulation results for different numbers of grid points. Parameters: $\delta = 0.01, D_n = 0.01$.